



11 **Abstract**

12       The CO<sub>2</sub> geo-sequestration has been studied as a countermeasure against global warming.  
13       When the injected CO<sub>2</sub> reacts with rock minerals, some portion may precipitate ultimately to  
14       carbonate minerals such as calcite and be trapped within the injected reservoir. It is of significant  
15       importance to examine how the mineral trapping exerts an influence on the mechanical, hydraulic,  
16       and transport properties in the targeted reservoir rocks because the trapped minerals may  
17       influence the integrity of the reservoir rocks, although such works are quite sparse in the  
18       literature. In this study, the influence of the mineral trapping on the evolution of the physical  
19       properties was evaluated by replicating the precipitation of calcite that may occur in the mineral  
20       trapping process. The calcite precipitation was enhanced artificially to occur within the void  
21       spaces of the Berea sandstone. Subsequently, the treated samples were examined by the  
22       mechanical and the permeability experiments. The experimental results revealed that  
23       approximately 10 % substitution of the void spaces by the precipitated calcite increased the  
24       modulus twofold and UCS by 20 %, and decreased the permeability by one order of magnitude,  
25       which should exert a favorable impact on the integrity of the reservoir against the leakage risks of  
26       the injected CO<sub>2</sub>. A cementation theory revealed the serial process of the calcite precipitation  
27       occurring on the free-surface of grains and at the grain contacts. The predictions of the  
28       permeability using the Kozeny-Carman equation clarified the increase of the surface roughness of

29 grains with the increase of the calcite precipitation.

30

31 **Keywords: CO<sub>2</sub> geo-sequestration, Mineral trapping, Calcite, Physical properties**

32

33 **Key Points:**

34 ➤ **Mineral trapping was simulated by in-situ calcite precipitation.**

35 ➤ **Mechanical properties were improved by the simulated mineral trapping.**

36 ➤ **Permeability decreased with the increase of precipitation.**

37 ➤ **Permeability was predicted using the Kozeny-Carman equation.**

38

## 39 **1. Introduction**

40 As is well known, the CO<sub>2</sub> geo-sequestration may be one of the solutions so as to mitigate  
41 the global warming. It is of significant importance to address coupled  
42 thermal-hydraulic-mechanical-chemical processes when considering the long-term underground  
43 isolation of anthropogenic CO<sub>2</sub>. The CO<sub>2</sub>-water-rock interactions should play an important role in  
44 assessing the CO<sub>2</sub> injectivity (Czernichowski-Lauriol et al., 1996; Fischer et al., 2013). As the  
45 injected CO<sub>2</sub> reacts with rock minerals, carbonate minerals such as calcite may precipitate as the  
46 secondary minerals, and occupy the pore spaces to some degree, which is called the mineral

47 trapping of CO<sub>2</sub> (Gunter et al., 1993; Bachu et al., 1994). Consequently, the mechanical and the  
48 hydraulic properties of the rocks should evolve. Thus, it is essential to examine quantitatively how  
49 such the mineral trapping exerts an influence on those properties. Due to the carbonate  
50 precipitation, the permeability of the host rocks may decrease and limit the extent of mineral  
51 reactions (Hövelmann et al., 2012), and the elasticity may be improved. The influence of the  
52 mineral trapping exerted on the evolution of the mechanical and the hydraulic properties may be  
53 significant. However, the direct observation of the mineral trapping is difficult because it is  
54 believed to be comparatively slow, maybe taking thousand years or even longer (IPCC, 2005).  
55 Therefore, the laboratory experiments focusing on the effect of the mineral trapping on those  
56 properties are quite sparse. Tarkowski et al. (2015) have conducted the 20-month experiments on  
57 brine-rock-CO<sub>2</sub> interactions to investigate the change of the petrophysical parameters due to the  
58 mineral trapping, concluding that the property of the reservoir rocks did not change significantly.  
59 However, the experimental period should be too short to fully understand the process of the  
60 mineral trapping and they have not examined the changes of the mechanical and the hydraulic  
61 properties.

62 To overcome the difficulty in directly observing the mineral trapping, the enhanced mineral  
63 trapping technique was proposed by Naganuma et al. (2011). In the system, bacteria were used to  
64 accelerate the carbonate precipitation, and the efficacy of the microbially induced carbonate

65 precipitation (MICP) was confirmed. Originally, the MICP has been applied in the geotechnical  
66 engineering to improve the deformation and strength properties of soils (Whiffin et al., 2007;  
67 Ivanov and Chu, 2008; Mitchell and Santamarina, 2005; DeJong et al., 2010; Harkes et al., 2010;  
68 van Paassen, 2011), and in the concrete engineering to improve the strength and durability of  
69 concrete and mortar (Qian et al., 2010; Achal et al., 2013). The research on the MICP has been  
70 mainly conducted using ureolytic bacteria (e.g., *Sporosarcina pasteurii*). These bacteria produce  
71 precipitated calcite by a urease enzyme. In this MICP technique, the transport and the fixation of  
72 the bacteria of interest are significant issues for achieving a suitable level of improvement of the  
73 saturated porous media, and thus, have been studied to this end (Murphy and Ginn 2000; Froppen  
74 and Shijven 2006; Whiffin et al. 2007; Harkes et al. 2010). In this work, the urease enzyme was  
75 adopted, instead of using bacteria, to accelerate the calcite precipitation, which was proposed by  
76 Yasuhara et al., (2012). Utilizing the enzyme itself is more straightforward than using bacteria,  
77 because the cultivation and fixation of bacteria (i.e., biological treatment) do not need to be  
78 considered. Again, in the MICP the microbial metabolism is a key factor, and it may be  
79 impossible to constrain the extinction and/or the generation of living bacteria in natural  
80 environments. In contrast, the enzyme-mediated calcite precipitation (EMCP) (Yasuhara et al.,  
81 2012; Neupane et al., 2013) can exclude the laborious biological treatments.

82 In this study, the evolution of the mechanical and the hydraulic properties in Berea sandstone

83 with initial porosity of  $\sim 0.23$  was examined quantitatively by replicating the mineral trapping  
84 process. The artificially accelerated mineral trapping was achieved by injecting the grouting  
85 materials (i.e., the EMCP technique), resulting in a rapid calcite precipitation within the pore  
86 spaces. The amount of the precipitated calcite can be controlled by changing the concentrations of  
87 the materials and the total injection volume. The measurements of the P-wave velocity, uniaxial  
88 compressive experiments, and the permeability experiments were conducted to examine the  
89 changes of the elasticity (i.e., the P-wave velocity and the elastic modulus), the uniaxial  
90 compressive strength, and the permeability due to the calcite precipitation. Note that in the  
91 mineral trapping process, several secondary carbonate minerals such as calcite ( $\text{CaCO}_3$ ), dolomite  
92 ( $\text{CaMg}(\text{CO}_3)_2$ ), siderite ( $\text{FeCO}_3$ ), and dawsonite ( $\text{NaAlCO}_3(\text{OH})_2$ ) may be precipitated (Xu et al.,  
93 2003), but the effect of calcite only was examined in this work.

94

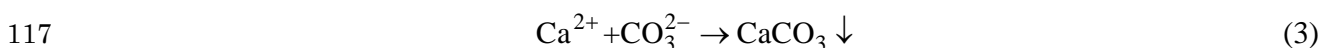
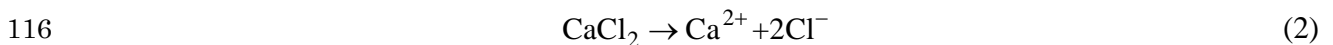
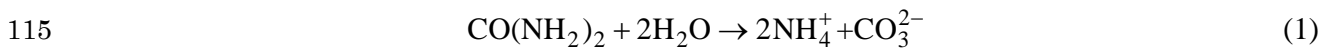
## 95 **2. Experimental methods**

### 96 *2.1. Rock samples and grout materials*

97 In this study, totally 47 cylindrical samples, whose names are called BS-1 – BS-47, 30 mm in  
98 diameter and 60 mm in height were made of a block of Berea sandstone (Fig. 1). Note that all the  
99 samples were cored parallel to the bedding planes, meaning that the flow direction of the grout  
100 injections and that in the permeability experiments were also parallel to them. It makes the grout

101 injections easier than being perpendicular to the bedding planes because the cores parallel to them  
102 have higher permeability. Before the grout injections, the initial porosity of all the samples were  
103 measured and was found to be ~0.23. The representative chemical compositions were determined  
104 by X-ray fluorescence (XRF) (Yasuhara et al., 2015a). The weight percentages of the major  
105 elements are listed in **Table 1**. In addition, the mineral compositions, before the grout injections,  
106 were also determined by X-ray diffraction (XRD) (Yasuhara et al., 2015b) and are shown in **Fig.2**.  
107 Berea sandstone is composed almost completely of pure quartz, but also contains slight amounts  
108 of feldspars, dolomite, and kaolinite.

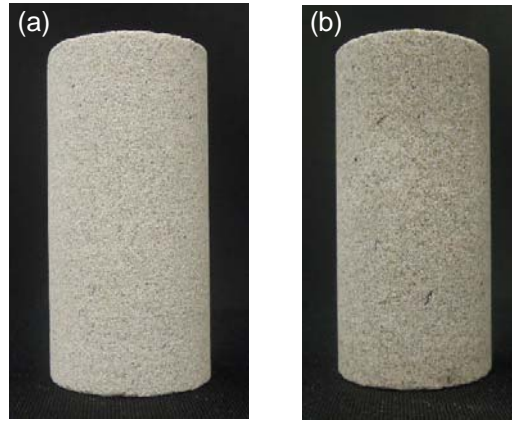
109 The grouting materials adopted in the EMCP technique are composed of urea, urease, and  
110 CaCl<sub>2</sub> (Yasuhara et al., 2012), and were injected in the samples to simulate the mineral trapping  
111 by the artificially-enhanced calcite precipitation. The urease, purified from the jack bean meal,  
112 having urease activity of 2950 U/g, has been used in the bio-catalytic dissociation of urea. The  
113 reactions to obtain the calcite precipitation, enhanced by the effect of urease, are expressed as  
114 follows,



118 where CO(NH<sub>2</sub>)<sub>2</sub> represents the urea. The urease was used to accelerate the reaction shown in Eq.

119 (1).

120



121

122 Fig. 1. Rock sample made of Berea sandstone ((a) before injection, (b) after injection).

123

124

125

Table 1. Composition of Berea sandstone (Yasuhara et al., 2015a).

Oxide	Results [wt.%]
SiO <sub>2</sub>	82.6
Al <sub>2</sub> O <sub>3</sub>	9.88
Fe <sub>2</sub> O <sub>3</sub>	2.13
SO <sub>3</sub>	-
K <sub>2</sub> O	1.97
CaO	1.66
MgO	0.973
Na <sub>2</sub> O	-
TiO <sub>2</sub>	0.633
Cl	-
Others	0.154

126

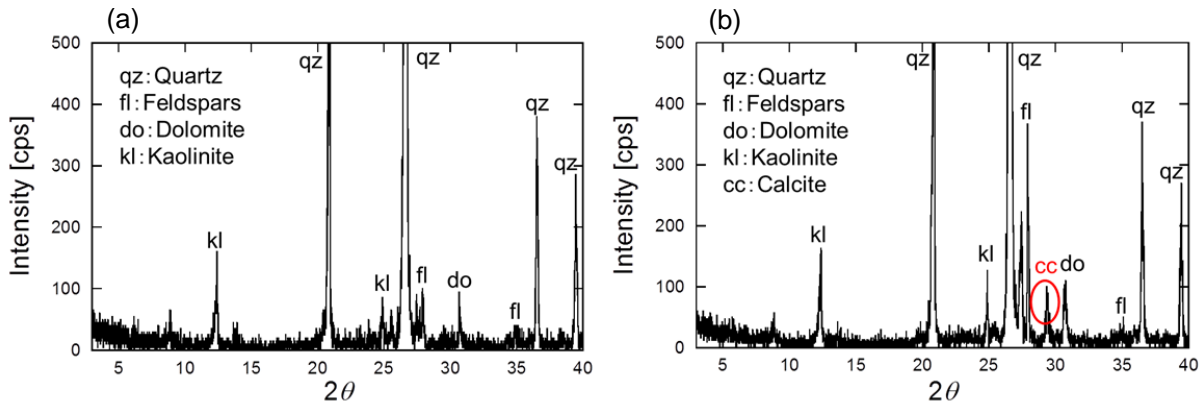
127

128

129

130

131



132

133

Fig. 2. Mineral composition of rock samples determined by XRD

134

((a) before injection, (b) after injection (BS-24)) (Yasuhara et al., 2015b).

135

## 136 2.2. Procedure of calcite precipitation

137

When simulating the mineral trapping by the calcite precipitation, uniform distribution of the

138

precipitation within the rock samples should be achieved to quantitatively investigate the change

139

of the mechanical and the hydraulic properties induced by the precipitation. To this end, an

140

organized procedure for injecting the grout materials was developed. Using the experimental

141

setup (Fig. 3) (Yasuhara et al., 2015b), the injections of the grout materials composed of urea,

142

urease, and  $\text{CaCl}_2$  were conducted by the following steps. Firstly, the rock samples were

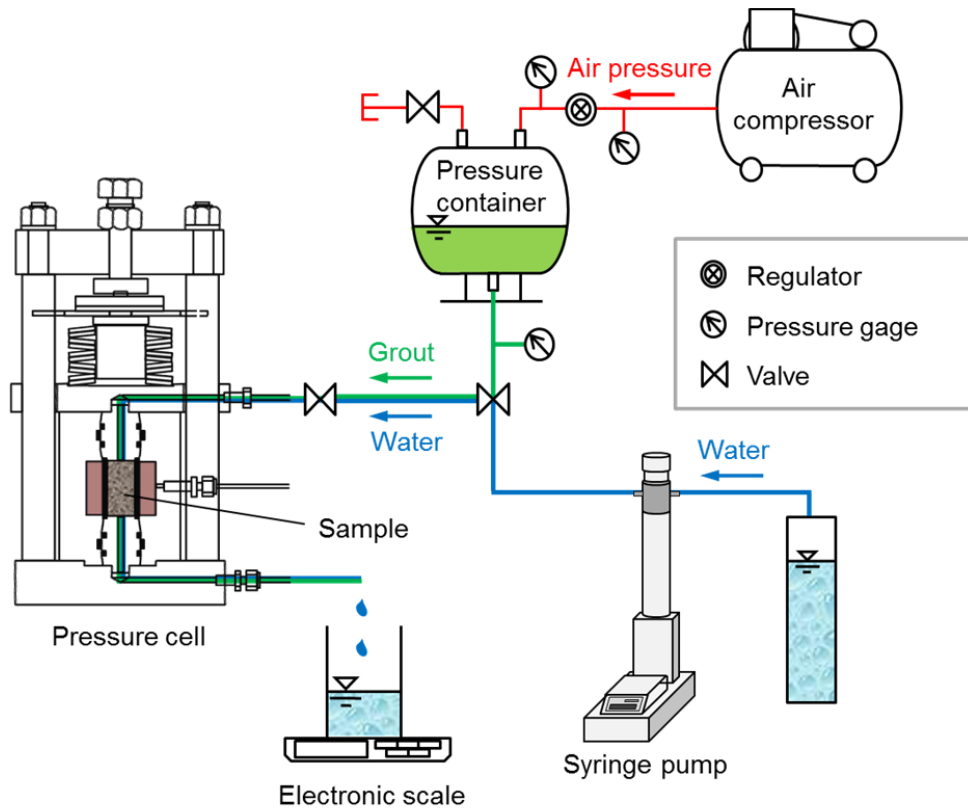
143

immersed in a beaker filled with de-ionized water and then placed inside a desiccator.

144 Subsequently, the space in the desiccator was evacuated by a vacuum pump for 24 hours in order  
145 to remove air from the rock samples. After the saturation process, the rock sample was confined  
146 within a heat-shrink tube. Once the core was jacketed, it was placed inside a pressure cell.  
147 Subsequently, axial pressure was prescribed by disc springs and controlled well by a load cell  
148 mounted onto the springs. Confining pressure, equivalent to the axial pressure, was applied by a  
149 hand pump and controlled by a regulator. In this work, 3 MPa was applied as the axial and the  
150 confining pressure to simulate the subsurface condition. Throughout the grout injections and the  
151 following permeability experiments were conducted under the pressure. After the rock sample  
152 was placed in the pressure cell, the concentration-adjusted grout materials were injected into the  
153 sample. The amount of each injection was 10 mL, which is roughly equivalent to the whole pore  
154 volume of each rock sample. Because the calcite precipitation starts within 30 minutes after the  
155 injection (Yasuhara et al., 2012), each injection was complete within 15 minutes. Then, the  
156 sample was placed quietly in the cell for 24 hours to wait for cease of the precipitation. After the  
157 24-hour curing time, de-ionized water was injected to flush the byproduct of  $\text{NH}_4\text{Cl}$  that is  
158 included in the grout materials (see Eqs. (1) and (2)). Note that it was confirmed that the  
159 byproducts was completely flushed out by the water injection. Subsequently, the above process  
160 was repeated as long as the grout injection could be complete within 15 minutes. Therefore, if the  
161 injection was not complete within the time, the injected grout was quickly flushed by de-ionized

162 water to avoid non-uniform precipitation within the rock samples.

163



164

165 Fig. 3. Experimental setup for grout injections and permeability experiments (Yasuhara et al.,  
166 2015b).

167

### 168 2.3. Petrographic and microstructural observations

169 The mineralogical alteration in the samples before and after the grout injections were

170 analyzed using XRD to identify the kinds of the precipitated minerals. The rock samples for the

171 XRD analyses were ground to obtain the powder samples. The ground particles were rinsed by

172 methanol for several times to remove the dusts remaining on the surfaces. Then, the particle  
173 samples were observed by XRD to identify the minerals and to examine the difference between  
174 the samples before and after the grout injections.

175 The microstructures of the rock samples were analyzed by an optical microscope to  
176 investigate the size and shape of the precipitated minerals. The rock samples were prepared by  
177 making a single fracture induced by the Brazilian tests. Then, fresh fracture surfaces opened by  
178 the tests were analyzed by the microscope. Two samples, one before the grout injections and the  
179 other after the injections, were observed to compare the differences. The pore size distributions of  
180 the samples before and after the grout injections were also observed by mercury porosimetry.  
181 Because the distributions may change due to the precipitation, the analysis results may be  
182 congruent with the microscope observations.

183 Another concern arising from the grout injections is whether a uniform distribution of the  
184 precipitation within the rock samples could be achieved. It is important to obtain the uniformity to  
185 examine the evolution of the mechanical and the hydraulic properties in the treated samples. If  
186 secondary minerals induced by the grout injections precipitate quite locally within the samples  
187 (e.g., concentrating close to the injection inlet), the relation between the amount of the  
188 precipitation and those properties evaluated through the experiments would be unreliable. To  
189 check the distribution of the precipitated minerals, a treated sample was cored by a core drill and

190 then, the core was cut by a saw to three pieces (**Fig. 4**). By evaluating the amount of the  
191 precipitation for the treated sample before cored, the three inner cores, and the cored outer sample,  
192 the precipitation distribution within the sample can be clarified.

193 As an index of evaluating the amount of precipitation within the samples, the pore  
194 occupation ratio,  $R_p$ , was defined by,

$$195 \quad R_p = \frac{V_c}{V_{v0}} \quad (4)$$

196 where  $V_c$  is the volume of the precipitated material ( $\text{m}^3$ ), and  $V_{v0}$  is the initial pore volume of the  
197 sample before the grout injections ( $\text{m}^3$ ). The pore volume,  $V_{v0}$ , can be obtained by calculating the  
198 porosity, given by,

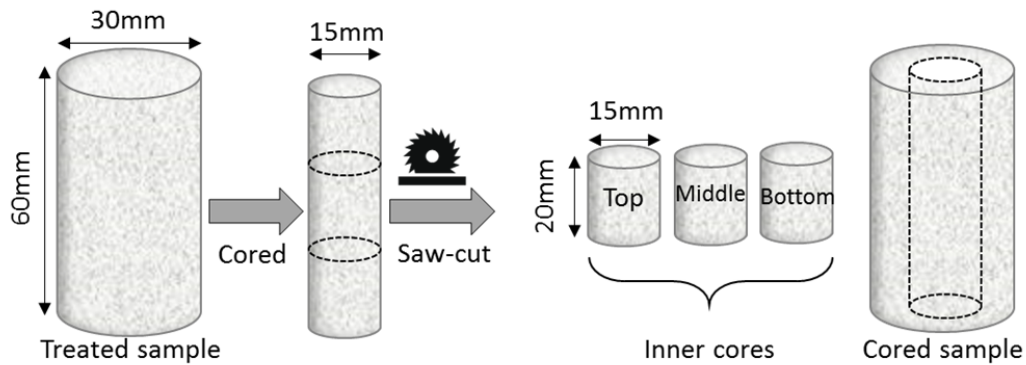
$$199 \quad \phi = \frac{\rho_g - \rho_d}{\rho_g} \quad (5)$$

$$200 \quad V_{v0} = \phi \cdot V \quad (6)$$

201 where  $\phi$  is the porosity of the sample (-),  $\rho_g$  is the grain density of the Berea sandstone (= 2700 kg  
202  $\text{m}^{-3}$ ), and  $\rho_d$  is the dry density of the samples ( $\text{kg m}^{-3}$ ). The evolution of the mechanical and the  
203 hydraulic properties were examined using this index in this work.

204

205



206

207 Fig. 4. Procedure to obtain the samples for examining the precipitation distribution.

208

209 *2.4. Mechanical experiments*

210 The P-wave velocity of the rock samples before and after the grout injections was measured  
 211 by a device. Prior to each measurement, the samples were completely dried within an oven at  
 212 60 °C for 8 hours. The velocity was measured three times for each measurement to avoid the  
 213 observation errors.

214 The uniaxial compression experiments were also conducted to obtain the elastic modulus and  
 215 the uniaxial compression strength (UCS) of the rock samples before and after the grout injections.  
 216 Two pieces of the two-axle strain gauges were pasted on the surface of the samples to measure the  
 217 vertical and horizontal strains. Then, the samples were set onto the compression table and the  
 218 displacement-controlled compression was statically conducted with the velocity of 0.10 mm s<sup>-1</sup>  
 219 until the failure. Subsequently, the UCS and the secant elastic modulus ( $E_{50}$  in this work) were  
 220 evaluated to examine the change of the mechanical properties induced by the mineral

221 precipitation.

222

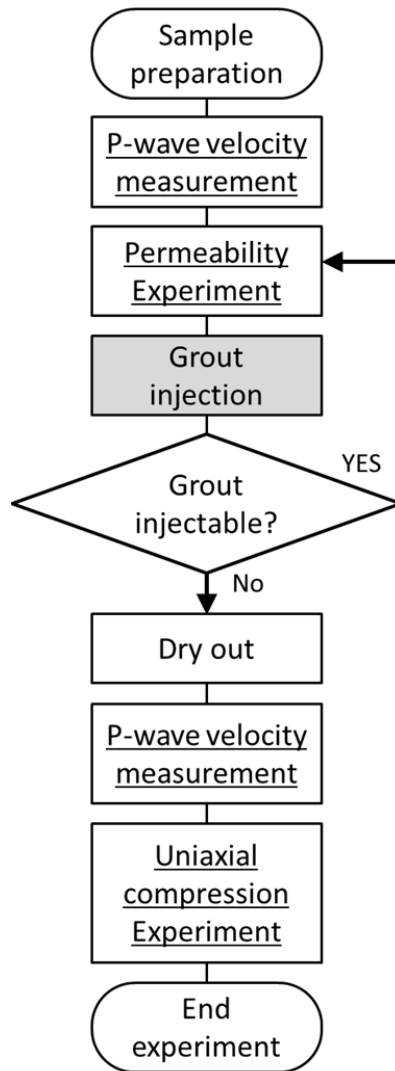
### 223 2.5. Permeability experiments

224 Permeability experiments using the setup as shown in **Fig. 3**, were conducted to obtain the  
225 relation between the pore occupation ratio and the measured permeability. Those were performed  
226 after each grout injection with the differential water pressure of 100 kPa. The permeability was  
227 evaluated by assuming a Darcian flow, given by,

$$228 \quad k = \frac{\mu QL}{A\Delta P} \quad (7)$$

229 where  $k$  is the intrinsic permeability ( $\text{m}^2$ ),  $\mu$  is the dynamic viscosity (Pa s),  $Q$  is the flow rate ( $\text{m}^3$   
230  $\text{s}^{-1}$ ),  $L$  is the sample height (m),  $A$  is the cross-sectional area ( $\text{m}^2$ ), and  $\Delta P$  is the differential water  
231 pressure (Pa). The measured permeability was also normalized by the initial values to examine the  
232 change of permeability with the pore occupation ratio. The procedure of the whole experiments  
233 including the grout injections, P-wave velocity measurements, permeability experiments, and  
234 uniaxial compression experiments can be depicted in **Fig. 5**.

235



236

237 Fig. 5. Procedure of whole experiments including grout injections, P-wave velocity measurements,

238 permeability experiments, and uniaxial compression experiments.

239

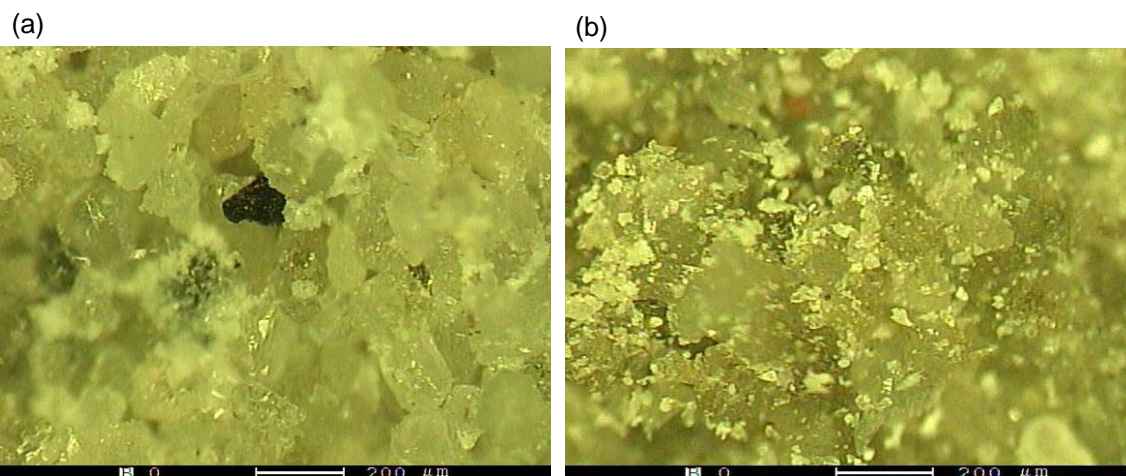
### 240 3. Experimental results

#### 241 3.1. Confirmation of calcite precipitation

242 Prior to showing the results of the mechanical and the permeability experiments, the calcite

243 precipitation was confirmed by the XRD analysis and the optical microscope observations, which  
244 was supplemented by the mercury porosimetry, and the distribution of the precipitated minerals  
245 within the samples was evaluated by the method shown in section 2.3. The obtained XRD patterns  
246 of the samples before and after the grout injections are shown in **Fig. 2**. As comparing the results  
247 between the pre- and post-injection samples, a clear, unique peak of calcite is apparent in the  
248 post-injection sample, and any other new peaks are not observed (**Fig. 2b**). Therefore, the  
249 precipitated mineral induced by the grout injections was confirmed to be calcite only. The  
250 photographs observed by the optical microscope are shown in **Fig. 6** (Yasuhara et al., 2015b). As  
251 is clearly seen in **Fig. 6b**, the white particles smaller than the sand particles with a diameter of  
252 approximately or more than 100  $\mu\text{m}$  (**Fig. 6a**), lie onto the sand particles, and these should be  
253 calcite. From this figure, the size of the calcite particles was found to range from several to a few  
254 tens of microns.

255



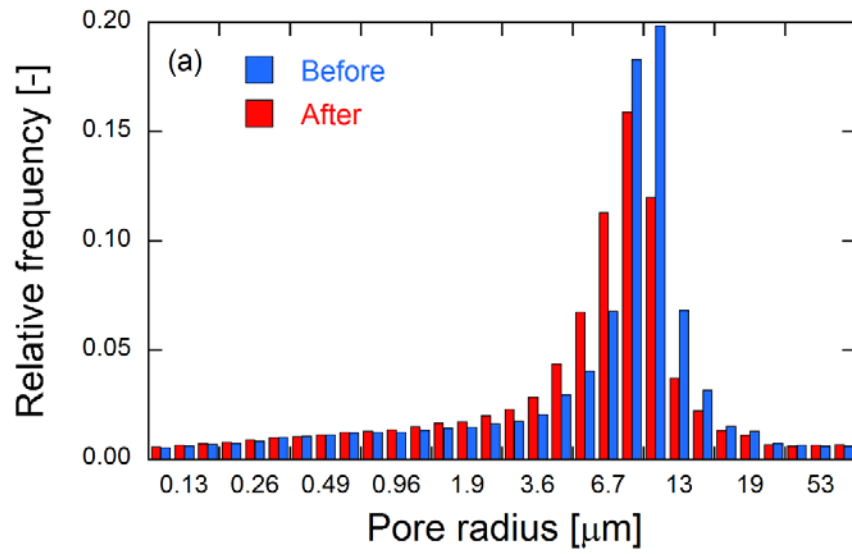
257 Fig. 6. Photographs of interior image of rock samples observed by optical microscope.

258 ((a) before injection, (b) after injection (BS-7)) (Yasuhara et al., 2015b).

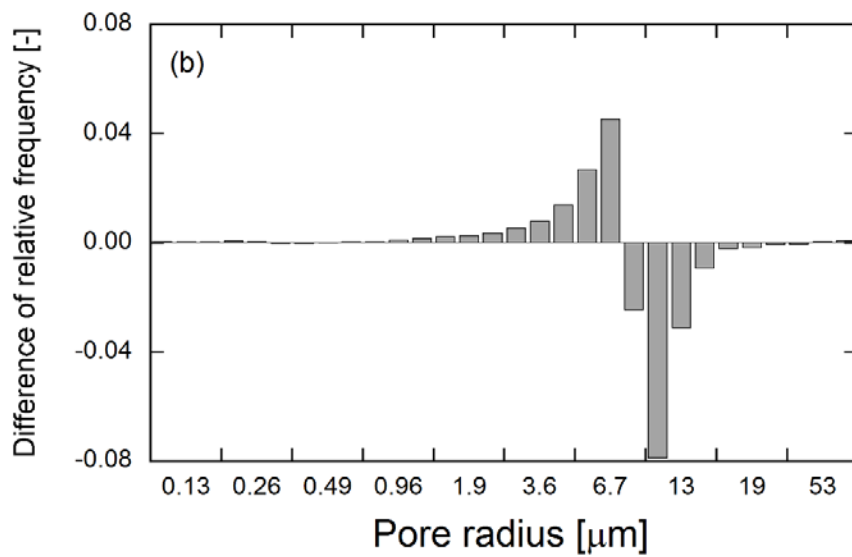
259

260 The pore size distribution of the samples before and after the calcite precipitation was  
261 analyzed by the mercury porosimetry (Fig. 7). Subtracting the frequency of the post-injection  
262 measurements from that of the pre-injection results in the difference of relative frequency (Fig.  
263 7b), clarifying how the pore radius distribution was changed by the calcite precipitation. Note that  
264 the positive and negative values in Fig. 7b represent the increase and the decrease of the relative  
265 frequency in the post-injection sample relative to the pre-injection, respectively. When comparing  
266 the pore radii of the pre- and post-injection samples, the pores with a radius of less than 6  $\mu\text{m}$   
267 increase and those with that of more than 6  $\mu\text{m}$  decrease in the post-injection sample. This is  
268 clearly attributed to the calcite precipitation. The results of the mercury porosimetry imply that the  
269 diameter of the precipitated calcite is a few tens of microns, which is congruent with the  
270 microscope observations.

271



272



273

274 Fig. 7. Pore radius frequency in rock samples obtained by mercury porosimetry. The sample of  
 275 BS-36 was used for the porosimetry after the experiments. ((a) relative frequency of pore radius,  
 276 (b) difference of relative permeability).

277

278 The distribution of the calcite precipitation within the sample was evaluated by following the

279 procedure described in section 2.3 (see **Fig. 4**). The porosity, the pore occupation ratio, and  
 280 P-wave velocity were obtained for the three inner cores and the cored outer sample, supplemented  
 281 with the measurements for the whole core before cored (**Table 2**). The obtained porosity, pore  
 282 occupation ratio, and P-wave velocity are relatively compatible among all of the measured  
 283 samples, although the pore occupation ratio of the top core is slightly lower than the others.  
 284 Consequently, it can be judged that relatively uniform distribution of the calcite precipitation was  
 285 achieved and the grouting method adopted in this work was reliable.

286

287 **Table 2.** Measurements of pore occupation ratio and P-wave velocity (BS-44).

Sample		Porosity (-)	Pore occupation ratio (-)	P-wave velocity (km s <sup>-1</sup> )
Inner cores	Top	0.233	0.055	2.91
	Middle	0.227	0.071	3.08
	Bottom	0.238	0.072	2.94
Cored sample		0.179	0.079	-
Average values		0.227	0.075	2.97
Whole sample before cored		0.224	0.082	2.96

288

### 289 3.2. Evolution in mechanical properties

290 The P-wave velocity was measured for the pre- and post-injection samples. The measured  
 291 velocity for the post-injection samples was normalized by that measured before the injections (**Fig.**  
 292 **8a**). A linear relation between the pore occupation ratio (see Eq. (4)) and the normalized P-wave

293 velocity was clearly obtained. The obtained relation shows that the P-wave velocity increases by  
 294 ~50 % when the pore occupation ratio reaches 0.10, which should exert a favorable influence on  
 295 the integrity of the CO<sub>2</sub>-injected reservoir against seismic motions. Using the measured P-wave  
 296 velocity, the dynamic elastic modulus can be evaluated by (Jaeger et al., 2007),

$$297 \quad E_D = \frac{V_p^2 \rho_d (1 + \nu_D)(1 - 2\nu_D)}{1 - \nu_D} \quad (8)$$

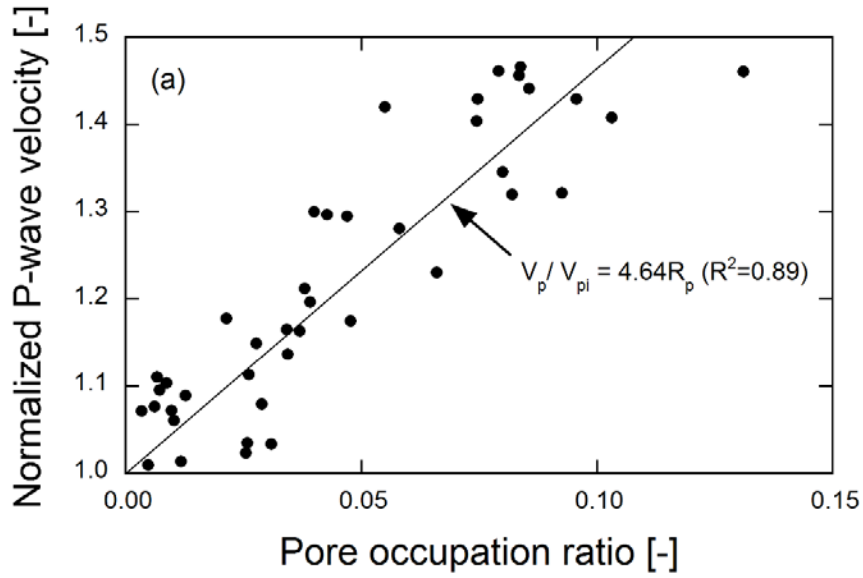
298 where  $E_D$  is the dynamic elastic modulus (Pa),  $V_p$  is the P-wave velocity (m s<sup>-1</sup>), and  $\nu_D$  is the  
 299 dynamic Poisson's ratio (-). As the S-wave velocity was not measured in this work, not only the  
 300 dynamic Poisson's ratio but also the dynamic elastic modulus cannot be directly evaluated.  
 301 However, the change of the modulus, which is the evolved modulus normalized by the initial  
 302 modulus of the pre-injection samples, may be able to be estimated by assuming the dynamic  
 303 Poisson's ratio and the dry density to be constant throughout the calcite precipitation, which can  
 304 be expressed as,

$$305 \quad \frac{E_D}{E_{D0}} = \left( \frac{V_p}{V_{p0}} \right)^2 \quad (9)$$

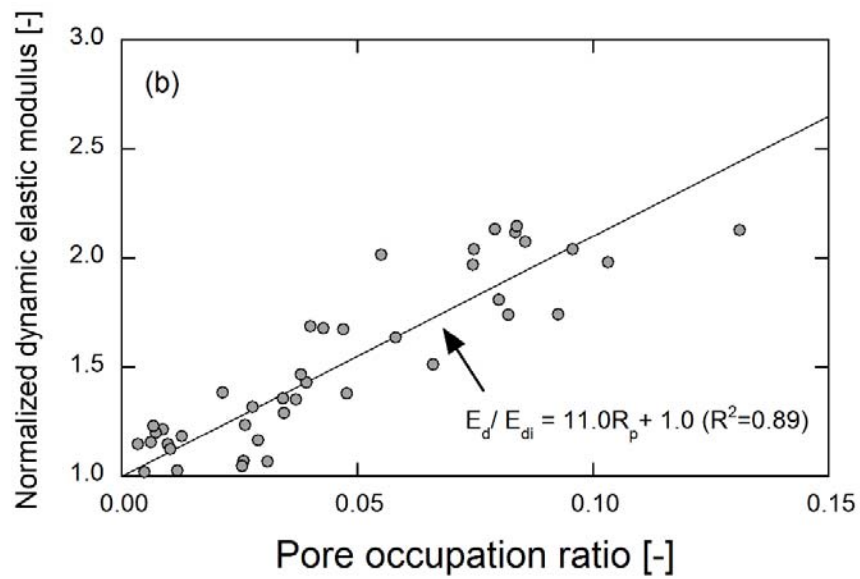
306 where  $E_{D0}$  is the initial dynamic elastic modulus (Pa) and  $V_{p0}$  is the initial P-wave velocity (m s<sup>-1</sup>)  
 307 before the calcite precipitation. The normalized dynamic elastic modulus evaluated by Eq. (9) is  
 308 shown in **Fig. 8b**. Similar to the measurements of the P-wave velocity (**Fig. 8a**), it linearly  
 309 increases with the increase of the pore occupation ratio and augments twofold when the pore

310 occupation ratio reaches 0.10.

311



312



313

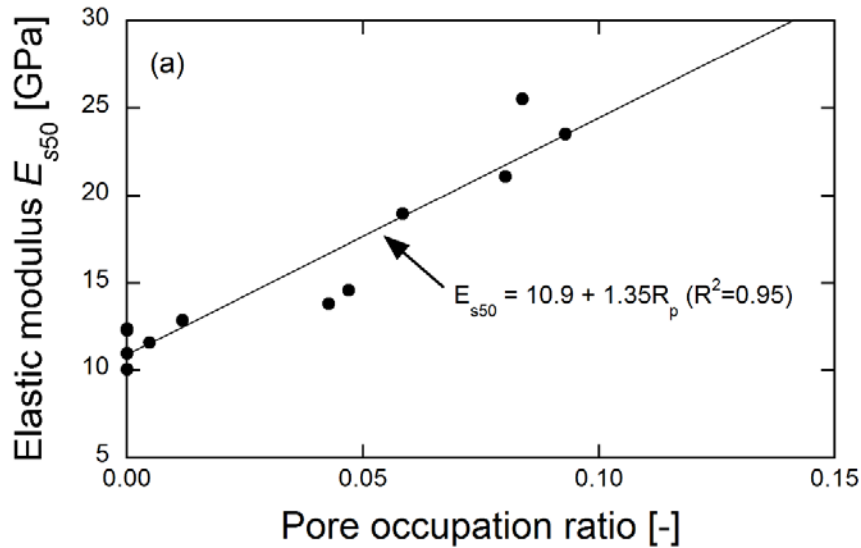
314 Fig. 8. Relation between pore occupation ratio and (a) normalized P-wave velocity and (b)

315 normalized dynamic elastic modulus.

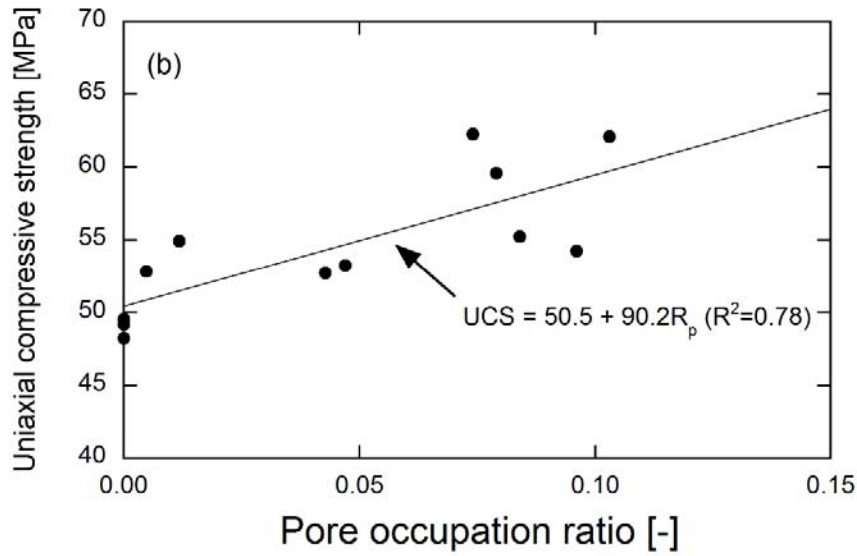
316

317 The uniaxial compression experiments were also conducted to examine the change of the  
318 mechanical properties induced by the calcite precipitation. The results of the experiments  
319 elucidate the evolution of the static elastic modulus and the UCS (**Fig. 9**). Both of the elastic  
320 modulus,  $E_{s50}$ , and the UCS increase linearly with the increase of the pore occupation ratio, and  
321 augment twofold and by 20 % when it attains 0.10, respectively. Note that the increasing rates of  
322 the dynamic and static elastic modulus (i.e.,  $E_D$  and  $E_{s50}$ ) coincide (see **Figs. 8b** and **9a**), and it  
323 can be thought that our measurements are reliable. The mechanical experiments revealed that  
324 clogging only the fraction of the pore spaces by the calcite precipitation significantly improves the  
325 deformation/strength characteristics.

326



327



328

329 Fig. 9. Relation between pore occupation ratio and (a) elastic modulus,  $E_{s50}$ , and (b) UCS.

330

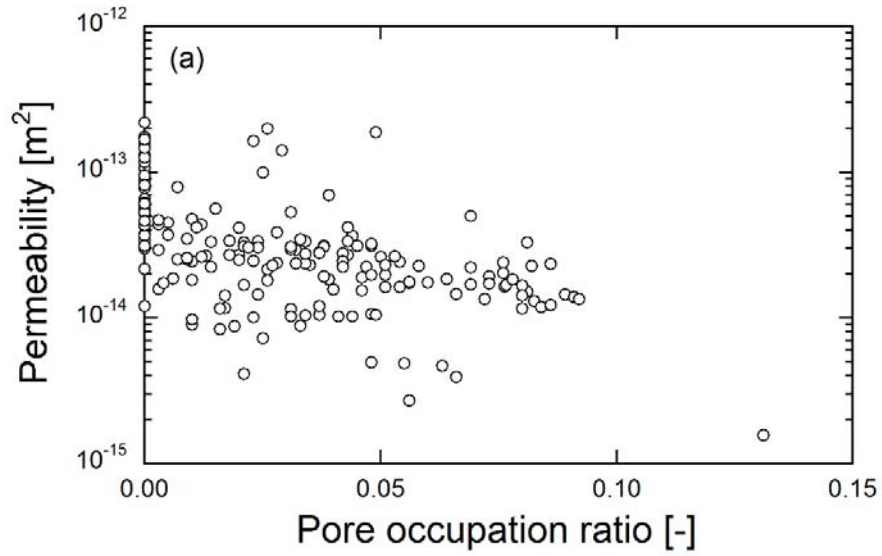
331 *3.3. Evolution in permeability*

332 The permeability experiments were conducted to examine the change of the permeability  
 333 induced by the calcite precipitation. The obtained permeability shows a decrease tendency with  
 334 the increase of the pore occupation ratio (**Fig. 10a**), but the tendency is ambiguous because of the  
 335 scattered data. Therefore, the measured permeability was initialized by the initial permeability  
 336 obtained before the grout injections (**Fig. 10b**). The normalization process made the decrease  
 337 tendency much clearer. The normalized permeability monotonically decreases with the increase of  
 338 the pore occupation ratio. Specifically, an abrupt decrease is observed after roughly 7 % - the  
 339 permeability at the occupation ratio of 9 % decrease by one order of magnitude. The reduction is

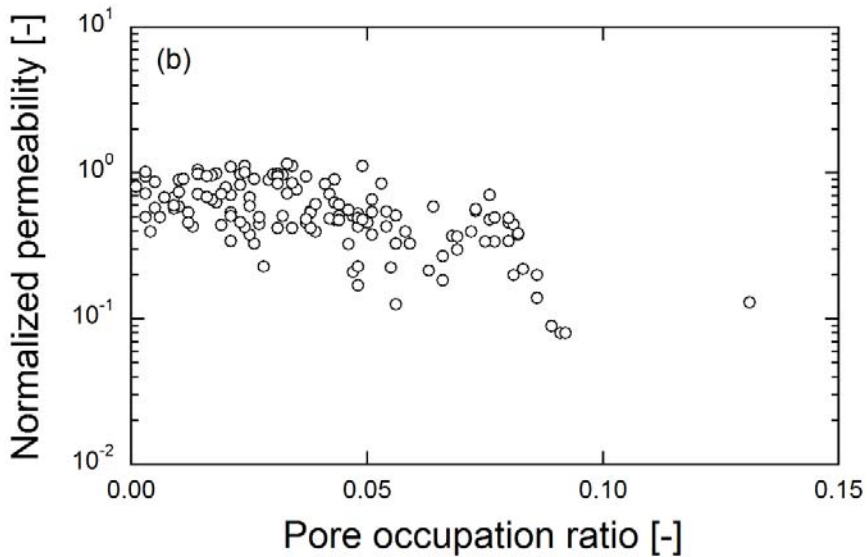
340 due to narrowing or clogging of the flow path by the calcite precipitation, which should also be

341 favorable to the confinement of the injected CO<sub>2</sub> in reservoirs.

342



343



344

345 Fig. 10. Relation between pore occupation ratio and (a) permeability and (b) normalized

346

permeability.

347

#### 348 **4. Discussion**

349 We have observed interesting results in the evolution of the mechanical and the hydraulic  
350 properties induced by the simulated mineral trapping (i.e., calcite precipitation) – the observed  
351 elastic modulus and the UCS increased with the increase of the calcite precipitation, while the  
352 permeability decreased with that. Firstly, to investigate the mechanisms of the change in elasticity,  
353 the P-wave velocity was estimated by following [Dvorkin and Nur \(1996\)](#). They model the P-wave  
354 velocity using a cementation theory where the grains mechanically interact through cement at the  
355 grain boundaries, given by,

$$356 \quad V_p = \sqrt{\frac{6K_{eff}}{n(1-\phi_0)\rho_c S_n}} \quad (10)$$

357 where  $K_{eff}$  is the effective bulk modulus (Pa),  $n$  is the average number of contacts per grain ( $n = 9$   
358 ([Dvorkin and Nur \(1996\)](#))),  $\rho_c$  is the density of the cement material, which is calcite in this work  
359 ( $= 2710 \text{ kg m}^{-3}$ ), and  $S_n$  is the fitting parameter (-).  $S_n$  is expressed as ([Dvorkin and Nur \(1996\)](#)),

$$360 \quad S_n = A_n(\Lambda_n)\alpha^2 + B_n(\Lambda_n)\alpha + C_n(\Lambda_n) \quad (11)$$

$$361 \quad A_n(\Lambda_n) = -0.024153 \cdot \Lambda_n^{-1.3646} \quad (12)$$

$$362 \quad B_n(\Lambda_n) = 0.20405 \cdot \Lambda_n^{-0.89008} \quad (13)$$

$$363 \quad C_n(\Lambda_n) = 0.00024649 \cdot \Lambda_n^{-1.9846} \quad (14)$$

364 
$$\Lambda_n = \frac{2G_c (1-\nu)(1-\nu_c)}{\pi G (1-2\nu)} \quad (15)$$

365 where  $\alpha$  is the ratio of the radius of the cement layer to the grain radius (-),  $G$  (Pa) and  $\nu$  (-) are  
 366 the shear modulus and the Poisson's ratio of the grains, respectively, and  $G_c$  (Pa) and  $\nu_c$  (-) are the  
 367 shear modulus and the Poisson's ratio of the contact cement layer, respectively. By assuming that  
 368 porosity reduction is caused only by cementation (i.e., calcite precipitation) and by adopting  
 369 certain schemes of cement deposition (**Dvorkin and Nur (1996)**), the ratio,  $\alpha$ , can be related to the  
 370 porosity amended by the calcite precipitation, as,

371 
$$\alpha = 2 \left[ \frac{\phi_0 - \phi}{3n(1-\phi_0)} \right]^{0.25} \quad (\text{Scheme 1}) \quad (16)$$

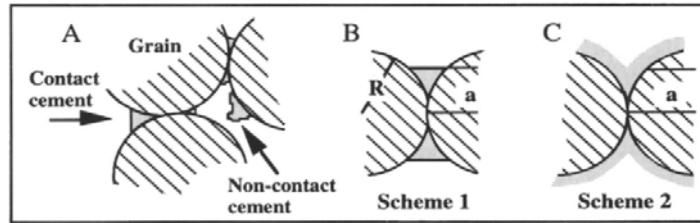
372 
$$\alpha = \left[ \frac{2(\phi_0 - \phi)}{3(1-\phi_0)} \right]^{0.5} \quad (\text{Scheme 2}) \quad (17)$$

373 where Schemes 1 and 2 are defined as the cases where all cement is deposited at grain contacts  
 374 and where cement is deposited evenly on the grain surface (**Fig. 11**). All the parameter values  
 375 used to estimate the P-wave velocity are summarized in **Table 3**. The model predictions of the  
 376 relation between the porosity and the P-wave velocity obtained by assuming the Scheme 1 or 2  
 377 are shown together with the experimental measurements (**Fig. 12a**), and those of the relation  
 378 between the pore occupation ratio and the P-wave velocity are depicted in **Fig. 12b**. Note that the  
 379 pore occupation ratio can be evaluated directly by the porosity, as,

380 
$$R_p = 1 - \frac{\phi}{\phi_0} \quad (18)$$

381 As is apparent, the measurements are followed by the model of the Scheme 2 in the early stage at  
 382 smaller calcite precipitation, and subsequently, those are followed by the Scheme 1. Therefore, the  
 383 pore occupation process is thought to be that the calcite precipitation firstly occurs on the  
 384 free-surface of the grains and that on the grain contacts dominate over the free-surface  
 385 precipitation.

386



387

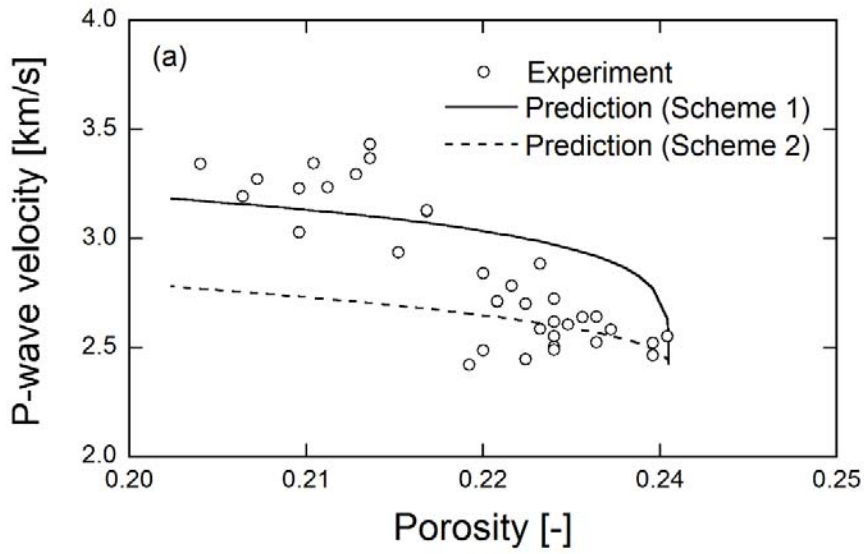
388 Fig. 11. Cemented grains ((a) Contact and noncontact cement, (b) Scheme 1 of cement deposition,  
 389 and (c) Scheme 2 of cement deposition) (Dvorkin and Nur, 1996).

390

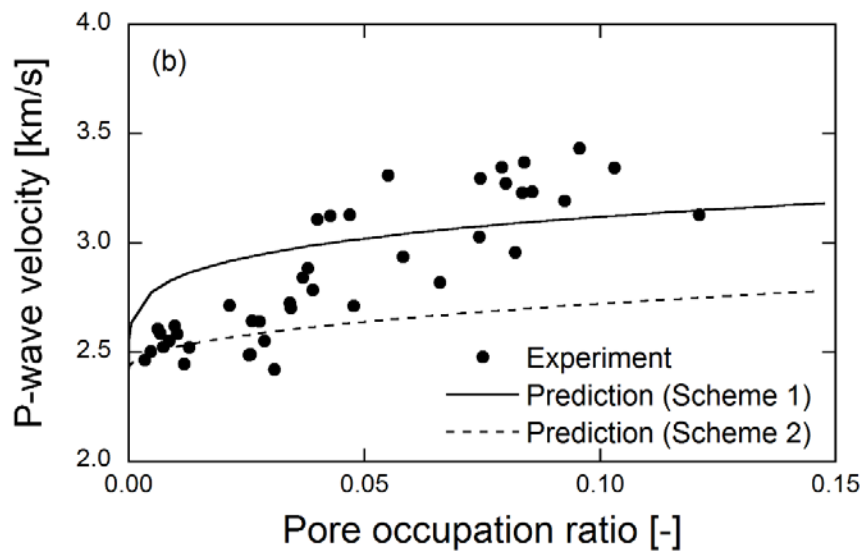
391 Table 3. Parameters in Eqs. (10)-(17) used to predict P-wave velocity.

$K_{eff}$ (GPa)	$n$ (-)	$\phi_0$ (-)	$\rho_c$ ( $\text{kg m}^{-3}$ )	$G$ (GPa)	$G_c$ (GPa)	$\nu$ (-)	$\nu_c$ (-)
11.9	9	0.235	2710	44.0	14.0	0.22	0.32

392



393



394

395 Fig. 12. Comparison between measurements and predictions of relation between P-wave velocity  
 396 and (a) porosity and (b) pore occupation ratio.

397

398 Secondly, to examine the mechanisms of the change in permeability, the experimental  
 399 measurements were predicted by the Kozeny-Carman equation (Bear, 1972), as,

400 
$$k = \frac{1}{5S_v^2} \frac{\phi^3}{(1-\phi)^2} \quad (19)$$

401 where  $S_v$  is the specific surface area ( $\text{m}^2 \text{m}^{-3}$ ). Eq. (19) can be rearranged with respect to the pore  
 402 occupation ratio using Eq. (18), as,

403 
$$k = \frac{1}{5S_v^2} \frac{\phi_0^3 (1-R_p)^3}{(1-\phi_0(1-R_p))^2} \quad (20)$$

404 Therefore, the permeability normalized by the initial permeability can be obtained as,

405 
$$\frac{k}{k_0} = \left( \frac{S_{v0}}{S_v} \right)^2 \frac{(1-R_p)^3 (1-\phi_0)^2}{(1-\phi_0(1-R_p))^2} \quad (21)$$

406 where  $k_0$  is the initial permeability ( $\text{m}^2$ ), and  $S_{v0}$  is the initial specific surface area ( $\text{m}^2 \text{m}^{-3}$ ). When  
 407 the calcite precipitation occurs on the free-surface and/or the contacts of grains, the specific  
 408 surface area should be changed. However, because it is clearly difficult to predict the change  
 409 through the precipitation, a simple relation, defined as  $S_v = S_{v0}(1+a \cdot R_p)$ , is assumed to follow  
 410 the measured permeability, and Eq. (21) can be rearranged as,

411 
$$\frac{k}{k_0} = \left( \frac{1}{(1+a \cdot R_p)} \right)^2 \frac{(1-R_p)^3 (1-\phi_0)^2}{(1-\phi_0(1-R_p))^2} \quad (22)$$

412 where  $a$  is the constant (-). When the parameter  $a$  is zero, the specific surface area never changes  
 413 from its initial value even if the calcite precipitation occurs. In contrast, when it is the positive or  
 414 negative value, the specific surface area increases or decreases with the increase of the pore  
 415 occupation ratio, respectively. As the calcite precipitation proceeds, the grain surface should be

416 rougher, which is supported by Fig. 6, and the specific surface area should increase accordingly.

417 Thus, the predictions with the positive values of  $a$  may result in better agreement with the

418 measurements. Actually, the experimental measurements are in disagreement with the prediction

419 as  $a = 0$ , while those are well-followed by the predictions with the positive values ranging from 5

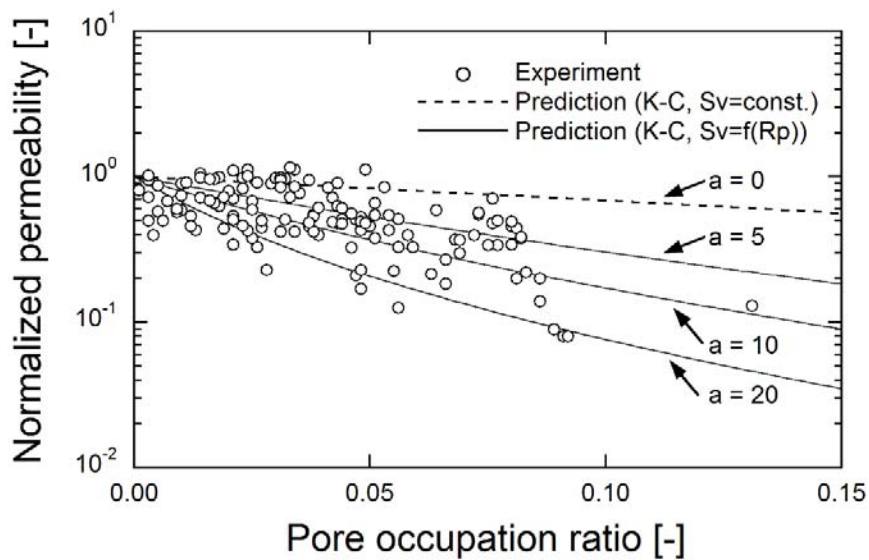
420 to 20 (Fig. 13). This indicates that the specific surface area may increase by 1.5 – 3 times as the

421 pore occupation ratio reaches 0.10. Therefore, to achieve reliable predictions of the permeability

422 change induced by the mineral trapping (i.e., carbonate precipitation), the change of the specific

423 surface area should also be estimated with a certain level of precision in advance.

424



425

426 Fig. 13. Comparison of relation between pore occupation ratio and normalized permeability

427 between measurements and predictions.

428

## 429 **5. Conclusions**

430 In this work, the evolution of the mechanical and the hydraulic properties were quantitatively  
431 examined by simulating the mineral trapping, which was achieved by the artificially-enhanced  
432 calcite precipitation using the EMCP technique. Before examining the change of those properties,  
433 uniform distribution of the calcite precipitation within the rock samples was confirmed by the  
434 XRD analyses, the optical microscope observations, the mercury porosimetry, and the direct  
435 measurements of the calcite amount.

436 Both of the estimated, normalized dynamic elastic modulus and the measured, static elastic  
437 modulus, and the UCS increased twofold and by ~20 % as the pore occupation ratio attained 0.10,  
438 respectively. The normalized permeability decreased by one order of magnitude at it reached 0.10.  
439 From the measurements of the mechanical and the permeability experiments, we understood that  
440 occupying the fraction of the pore spaces dramatically exerts favorable influences on the integrity  
441 of the CO<sub>2</sub>-injected reservoir.

442 A cementation theory proposed by [Dvorkin and Nur \(1996\)](#) enabled us to understand where  
443 the calcite selectively precipitated within the domain – firstly, the precipitation may have occurred  
444 evenly on the grain surface, and gradually it concentrated at grain contacts, resulting in the  
445 significant augmentation of the mechanical properties. The predictions by the Kozeny-Carman

446 equation verified that the grain surface became rougher due to the calcite precipitation, and  
447 showed that the specific surface area likely increased by 1.5 to 3 times as the pore occupation  
448 ratio reached 0.10. We have conducted a series of the experiments to understand quantitative  
449 evolutions of the physical properties. Although interesting and valuable results were obtained  
450 from the experiments, the obtained pore occupation ratio was at most 0.10, and higher ratios  
451 should have been attained. As a future study, by improving the grout injection technique, the  
452 mechanical and the hydraulic properties at the pore occupation ratios much greater than 0.10 will  
453 be investigated quantitatively to unravel the influences of the mineral trapping on those  
454 properties.

455

#### 456 **Acknowledgement**

457 This work has been partly supported by research grant from the Research Foundation for the  
458 Electrotechnology of Chubu, Nagoya, Japan. Their support is gratefully acknowledged. The  
459 authors also thank Mr. Ryota Kashiwagi, Ms. Tomomi Ishimizu and Mr. Hiroki Okahata for their  
460 help with the experimental portion of this study.

461

462

463

464

465

466 **6. References**

- 467 Achal, V., Mukerjee, A., Sudhakara Reddy, M., 2013. Biogenic treatment improves the durability  
468 and remediates the cracks of concrete structures. *Constr. Build. Mater.*, 48, 1–5.
- 469 Bear, J., 1972. *Dynamics of Fluids in Porous Media*, Dover Publications, Inc., p. 166.
- 470 Bachu, S., Gunter, W. D., Perkins, E. H., 1994. Aquifer disposal of CO<sub>2</sub>: Hydrodynamic and  
471 mineral trapping, *Energy Convers. Manag.*, 35, 269–279.
- 472 Czernichowski, I., Sanjuan, B., Rochelle, C., Bateman, K., Pearce, J. M., Blackwell, P., 1996.  
473 Analysis of the geochemical aspects of the underground disposal of CO<sub>2</sub>, in: Apps, J.A.,  
474 Tsang, C.F. (Eds.), *Deep Injection Disposal of Hazardous and Industrial Waste: Scientific and*  
475 *Engineering Aspects*. Academic Press, New York, pp. 565–583.
- 476 DeJong, J. T., Mortensen, B. M., Martinez, B. C., Nelson, D. C., 2010. Bio-mediated soil  
477 improvement. *Ecol. Eng.*, 36, 197–210.
- 478 Dvorkin, J., Nur, A., 1996. Elasticity of high-porosity sandstones: Theory for two North Sea data  
479 sets, *Geophysics*, 61, 1363–1370.
- 480 Fischer, S., Liebscher, A., De Lucia, M., Hecht, L., & The Ketzin Team., 2013. Reactivity of  
481 sandstone and siltstone samples from the Ketzin pilot CO<sub>2</sub> storage site—laboratory  
482 experiments and reactive geochemical modeling. *Environ. Earth Sci.*, 70, 3687–3708.
- 483 Foppen, J. W. A., Schijven, J. F., 2006. Evaluation of data from the literature on the transport and

484 survival of *Escherichia coli* and thermotolerant coliforms in aquifers under saturated  
485 conditions. *Water Res.* 40, 401–426.

486 Gunter, W. D., Perkins, E. H., McCann, T. J., 1993. Aquifer disposal of CO<sub>2</sub>-rich gases: reaction  
487 design for added capacity. *Energy Convers. Manage.* 34, 941–948.

488 Harkes, M. P., van Paassen, L. A., Booster, J. L., Whiffin, V. S., van Loosdrecht, M. C. M., 2010.  
489 Fixation and distribution of bacterial activity in sand to induce carbonate precipitation for  
490 ground reinforcement. *Ecol. Eng.*, 36, 112–117.

491 Hövelmann, J., Austrheim, H., Jamtveit, B., 2012. Microstructure and porosity evolution during  
492 experimental carbonation of a natural peridotite. *Chem. Geol.* 334, 254–265.

493 Intergovernmental Panel on Climate Change (IPCC), 2005. Special Report on Carbon Dioxide  
494 Capture and Storage, in: Metz, B, Davidson, O, de Coninck, H. Loos, M., Meyer, L. (Eds.),  
495 Underground geological storage. Cambridge University Press, New York, pp. 195–276.

496 Ivanov, V., Chu, J., 2008. Applications of microorganisms to geotechnical engineering for  
497 bioclogging and biocementation of soil in situ. *Rev. Environ. Sci. Biotechnol.*, 7, 139–153.

498 Jaeger, J. C., Cook, N. G. W., Zimmerman, R. W., 2007. Fundamentals of rock mechanics, fourth  
499 ed. Blackwell Publishing, Malden, MA.

500 Mitchell, J. K., Santamarina, J. C., 2005. Biological considerations in geotechnical engineering. *J.*  
501 *Geotech. Geoenviron. Eng.*, 131, 1222–1233.

502 Murphy, E. M., Ginn, T. R., 2000. Modeling microbial processes in porous media. *Hydrogeol. J.*,  
503 8, 142–158.

504 Naganume, T., Yukimura, K., Todaka, N., Ajima, S., 2011. Concept and experimental study for a  
505 new enhanced mineral trapping system by means of microbially mediated processes, *Energy*  
506 *Procedia*. 4, 5079–5084.

507 Neupane, D., Yasuhara, H., Kinoshita, N., Unno, T., 2013. Applicability of enzymatic calcium  
508 carbonate precipitation as a soil-strengthening technique, *ASCE, J. Geotech. Geoenviron.*  
509 *Eng.*, 139, 2201–2211.

510 Qian, C., Wang, R., Cheng, L., Wang, J., 2010. Theory of microbial carbonate precipitation and its  
511 application in restoration of cement-based materials defects. *Chin. J. Chem.*, 28, 847–857.

512 van Paassen, L. A., 2011. Bio-mediated ground improvement: from laboratory experiment to pilot  
513 applications. *Geo-Frontiers 2011, ASCE*, 4099–4108.

514 Whiffin, V. S., van Paassen, L. A., Harkes, M. P., 2007. Microbial carbonate precipitation as a soil  
515 improvement technique. *Geomicrobiol. J.*, 24, 417–423.

516 Xu, T., Apps, J. A., Pruess, K., 2003. Reactive geochemical transport simulation to study mineral  
517 trapping for CO<sub>2</sub> disposal in deep arenaceous formations. *J. Geophys. Res.* 108(B2), 2071,  
518 doi:10.1029/2002JB001979.

519 Yasuhara, H., Neupane, D., Hayashi, K., Okamura, M., 2012. Experiments and predictions of

520 physical properties of sand cemented by enzymatically-induced carbonate precipitation. *Soils*  
521 *Found.*, 52, 539–549.

522 Yasuhara, H., Kinoshita, N., Ohfuji, H., Takahashi, M., Ito, K., Kishida, K., 2015a. Long-term  
523 observation of permeability in sedimentary rocks under high-temperature and stress  
524 conditions and its interpretation mediated by microstructural investigations, *Water Resour.*  
525 *Res.*, 51, doi:10.1002/2014WR016427.

526 Yasuhara, H., Kashiwagi, R., Kinoshita, N., Lee, D. S., Kishida, K., 2015b. Evaluation of  
527 mechanical and hydraulic properties by laboratory experiments simulating mineral trapping  
528 of CO<sub>2</sub> sequestration. *J. MMIJ*, 131, 497–502.

529

530

531